Applied Catalysis B: Environmental 95 (2010) 14–25

Contents lists available at ScienceDirect

Applied Catalysis B: Environmental

journal homepage: www.elsevier.com/locate/apcatb

Decomposition of 2-chlorophenol employing goethite as Fenton catalyst II: Reaction kinetics of the heterogeneous Fenton and photo-Fenton mechanisms

Guadalupe B. Ortiz de la Plata *, Orlando M. Alfano, Alberto E. Cassano

INTEC (Universidad Nacional del Litoral and CONICET), Colectora de la Ruta Nacional No. 168, Km 472.5, (3000) Santa Fe, Argentina

ARTICLE INFO

Article history:
Received 17 May 2009
Received in revised form 4 December 2009
Accepted 4 December 2009
Available online 16 December 2009

Keywords:
AOT
Heterogeneous
Fenton and photo-Fenton
Reaction kinetics
Goethite
2-Chlorophenol

ABSTRACT

The kinetics of the degradation of 2-chlorophenol (2-CP) employing both the heterogeneous Fenton and photo-Fenton reactions using goethite as the solid catalyst is studied. The photoreactor was irradiated with a 350–400 nm wavelength light. The kinetics is based on 19 steps of a combined heterogeneous–homogeneous mechanism derived for the thermal Fenton reaction [see companion article by the authors: Ortiz de la Plata et al. (2009)] [1]. For the photo-Fenton alternative, two more steps are needed. Some of the specific kinetic constants of the reaction scheme are approximately known. However, for the heterogeneous "thermal" Fenton reaction, three new unknown constants were required and were attained from experimental data obtained in this and the previous work. The parameters were (i) the reaction of the $HO^{\bullet}$ radical with 2-CP, (ii) the proton induced iron dissolution and (iii) the reductive induced iron dissolution [1]. In the case of the heterogeneous photo-Fenton reaction steps, the radiation field in the reacting system was described by solving the complete radiative transfer equation inside the reactor. With this purpose, the knowledge of the needed goethite optical properties were previously characterized [2]. Combining the dark and the irradiated experiments 21 kinetically consistent parameters were achieved for the proposal of a feasible mechanism. They are valid for both systems; making the two primary quantum yields of the photoreaction equal to zero, the "dark" Fenton reaction performance is properly described by the remaining 19 specific rate constants. These results are independent of the used experimental apparatus and can be safely used for scaling-up purposes within the range of the explored variables.

1. Introduction

In spite of the efforts made in the last decades, environmental pollution is still a serious problem of the modern world. New methods to remediate the damage produced by inappropriate human activities are needed. Among them, Advanced Oxidation Technologies seem to open a potential alternative, especially for their broad applicability and the possibility of full destructive characteristics. Some of them are specifically identified by the use of UV radiation, for example: hydrogen peroxide + UVC, Ozone + UVC, Titanium dioxide photocatalysis and different variations of the Fenton reaction. Precisely, one of the most promising alternatives is the Fenton reaction with its feasibility of increasing its efficiency by rising the temperature and the enhancement resulting by the application of UV–visible radiation, both achievable with the use of solar radiation. In the past fifteen years, to reduce post-treatment costs by eliminating as much as possible dissolved iron, various researchers in the field explored the prospect of using heterogeneous Fenton and photo-Fenton processes, which has stimulated active research towards this direction [3–6]. Some other examples include studies by Pignatello et al. [7] and literature cited therein [8–11], just to mention some of the most recent contributions.

The heterogeneous Fenton process uses H_2O_2 and employs iron immobilized on a large variety of solid supports [2]. Alternatively, it can employ particles of iron oxides. Among the latter, goethite seems to be very attractive and its main advantages have been described in reference [2]. A more complete, although non-exhaustive, review on previous reports has been made by the authors [1,2].

Compared with Fenton and photo-Fenton reaction studies in homogeneous systems, there is not equivalent information

Abbreviations: 2-CP, 2-chlorophenol; ClBQ, chlorobenzoquinone; ClHQ, chlorohydroquinone; ClSQ, chlorosemiquinone; LVRPA, the local volumetric rate of photon absorption (Einstein $cm^{-3}\,s^{-1}$); ODE, ordinary differential equation; RTE, the radiative transfer equation.

* Corresponding author. Tel.: +54 342 4511546; fax: +54 342 4511087.
E-mail addresses: guadaortiz@santafe-conicet.gov.ar, guadaortiz@yahoo.com.ar (G.B.O. de la Plata).

0926-3373/$ – see front matter © 2009 Elsevier B.V. All rights reserved.
doi:10.1016/j.apcatb.2009.12.006

regarding the models of complete mechanisms or rigorous, mechanistically based, kinetics studies for heterogeneous Fenton or photo-Fenton reactions. This is also true for their applications to pollutant degradation [4–7]. Much work is still needed in order to transform the heterogeneous Fenton and photo-Fenton operation into an efficient process suitable for practical applications. Just recently, Ortiz de la Plata et al. [see the companion article by the authors [1]] performed a study on the development of a rigorous model of the reaction mechanism for the decomposition of 2-chlorophenol (2-CP) employing small particles of goethite (75–150 μm) as Fenton catalyst. It was based on a combined scheme of heterogeneous and homogeneous reactions carried out a pH 3 ± 0.1. This work describes three heterogeneous and two homogeneous combined mechanisms to explain the observed behavior. The heterogeneous reactions are: (i) The known mechanism leading to the unusual consumption of hydrogen peroxide (H_2O_2) [12], (ii) the proton promoted iron dissolution and (iii) the 2-CP quinone byproducts promoted reductive iron dissolution. The homogeneous reactions are: (i) The classical scheme of the homogeneous Fenton reaction [7] and (ii) the enhancement of the $Fe^{3+} \rightarrow Fe^{2+}$ cycle, produced by quinone derivatives proposed by Chen and Pignatello [13]. Based on a selected set of experiments, reference [1] proposed a 19 step reaction scheme. The work was conducted at different temperatures between 25 and 50 °C. The size of the particles was a compromising solution between a fast settling post-treatment process and the improvement of the light transmission characteristics of the solid suspension on one hand, and the existence of several very important solid-liquid heterogeneous reactions that always depend on the available surface area, on the other hand.

The pH was chosen after the analysis of different results published in the literature with values varying between 3 and 10 as can be seen in the references mentioned before. Iron leaching never exceeded 4.3 mg L^{-1} at the highest employed temperature (50 °C) after 6 h of reaction time. A catalyst loading of 0.5 g L^{-1}, an initial molar ratio of H_2O_2/2-CP between 40 and 50 and a temperature of 50 °C were found to be the best operating conditions. The present work reports a mechanistically derived study of the kinetics of the Heterogeneous Fenton and photo-Fenton reaction at 25 °C. In the case of the photo-Fenton process, the previously mentioned reaction scheme must be complemented with the additional steps resulting from the participation of photons in a photochemical reaction that, in this case, is carried out in a heterogeneous medium. Thus, radiation absorption by all the soluble components, plus absorption and scattering produced by the goethite particles, must be taken into account. The necessary information on the optical properties of the employed goethite was measured before [2]. As might be anticipated, a significant number of kinetic constants for the homogeneous Fenton and photo-Fenton reaction have been already published by different authors; unfortunately, they are only known at 25 °C and in most of the cases, the corresponding errors within a given confidence interval have not been reported. Hence, in a first stage, experiments will be aimed at obtaining, at this temperature, all the missing reaction specific rate constants, resorting to the laboratory data, the derived tentative kinetic scheme, a complete heterogeneous reactor model, and a non-linear multi-parameter estimation program. The already known constants will be accepted as such or used as the best initializing values for calculations. The expected final output is the entire set of kinetic constants of the proposed combined heterogeneous–homogeneous reaction scheme. Once obtained, this set will be used in a simulation program based on the same heterogeneous reactor model. The kinetic constants should be able to show within an acceptable error, good agreement with the whole set of experimental data. In addition, another demand will be imposed. They will be required to be valid either for results corresponding to the Fenton or to the photo-Fenton reaction, with the simple operation of excluding, in the first case, all those steps that involve the use of UV–visible radiation.

2. Materials and methods

2.1. Model compound, employed chemicals and analytical methods

All the information was included in Part 1 (reference [1]). It will not be repeated here.

2.2. Optical properties of goethite catalyst

In the case of the heterogeneous photo-Fenton reaction there are several components that may absorb radiation; specifically iron compounds, reaction byproducts such as some chloroquinone derivatives and the solid catalyst. For the species in solution, the knowledge of the radiation absorption coefficient can be obtained from published values or conventional absorbance measurements in a spectrophotometer. The case of the catalyst is different, because it will absorb and scatter photons. Neither are these properties usually known nor are they very simple to measure. For the radiation model to be used in the photo-Fenton process reactor (Section 4.4.1), the optical properties of the employed catalyst must be indispensably known. They are the specific (per unit mass) spectral absorption (κ^*_λ) and the specific (per unit mass) spectral scattering (σ^*_λ) coefficients, as well as the asymmetric factor of the employed phase function for scattering (in our case, the adopted Henyey and Greenstein model [14]). All of them must be known as a function of wavelength. They were obtained in [2] and Table 1 shows only the specific part of those results that are required for this work, considering that the useful wavelength range (see below) is encompassed in the interval that goes from 350 to 400 nm. The details of the method can be seen on the cited reference.

2.3. The reactor

The work was performed in a cylindrical, well-stirred, batch reactor irradiated from a transparent radiation bottom, which was illuminated with a tubular lamp placed at the focal axis of a parabolic reflector (Fig. 1 and Table 2). The stirrer was custom built, made of polymethylmethacrylate, with blades producing axial and upwardly directed flow. Stirring was very intense in order to ensure permanent saturation of the solution by the oxygen produced by the reaction. The reactor was also equipped with internal transparent glass heat exchangers connected to a thermostatic bath for temperature control and, at the same time, to act as baffles in order to preclude non-uniform distribution of the catalyst particles. External insulation was made of K-Wool. As shown in Fig. 2, ≈95% of the lamp emission was in the range from 350 and 400 nm. Within this range, the reflectivity of the parabolic

Table 1
Goethite specific absorption and scattering coefficients as well as the asymmetry factor.

Optical properties of goethite (Aldrich) [($L_{Part.}$ = 75–150 μm), (S_g = 141 $m^2 g^{-1}$), (V_{Pore} = 0.22 $cm^3 g^{-1}$), ($D_{Pore,aver.}$ = 6.1 nm)]			
λ (nm)	κ^*_λ ($cm^2 g^{-1}$)	σ^*_λ ($cm^2 g^{-1}$)	g_λ[a]
350	97	46	0.881
360	107	41	0.891
370	115	38	0.883
380	115	40	0.887
390	108	56	0.888
400	102	59	0.888

[a] Asymmetric factor of the Henyey and Greenstein model [14] $0 < g \leq 1$ for forward scattering, $-1 \leq g < 0$ for backward scattering. $g = 0$ for isotropic scattering.

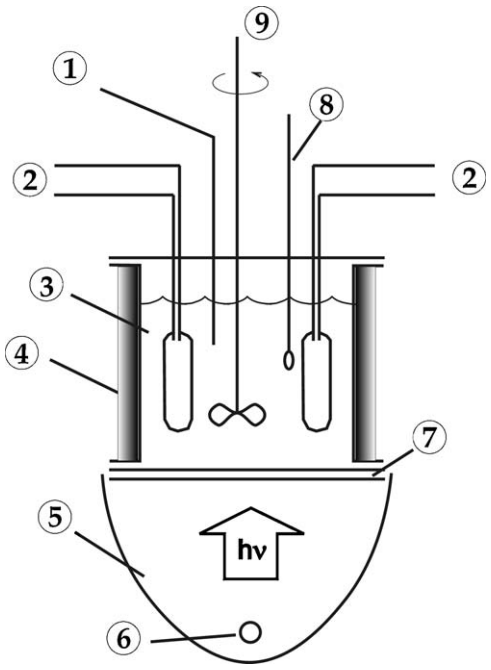

Fig. 1. (1) Sampling port, (2) temperature control, (3) reactor, (4) K-wool insulation, (5) parabolic reflector, (6) lamp, (7) double wall window, (8) thermometer and (9) stirrer.

reflector is constant. The same figure shows the transmission characteristics of the polymethylmethacrylate plate and the borosilicate ground glass placed at the reactor bottom that is needed for simplifying the radiation model. When the ground glass is placed underneath, it produces diffuse radiation entrance, which renders azimuthal symmetry to the radiation beam that must be mathematically described in the heterogeneous reacting medium. The radiation input to the reactor wall can be changed with specially constructed neutral density filters made of UVA transparent, 0.25 mm thin films of biaxially oriented polyethylene terephthalate that are printed with a Corel Draw program that permits to obtain different hues of grays [15]. A 48% transmittance almost constant for the wavelength of interest was obtained (data are also shown in Fig. 2).

2.4. Operation

The reactor was filled with distilled water and the desired concentration of goethite. Then, 2-CP was added to reach an intended initial concentration of 0.39 mM (50 ppm). After reaching steady-state temperature (and for the photo-Fenton process also lamp irradiation steady operation), pH was adjusted with perchloric acid according to the details and considerations made in [1]. Then, the prescribed H_2O_2 was incorporated to the system. For irradiated runs, a shutter was interposed between the reactor bottom and the irradiating system, which was removed when the steady state operation of the lamp was achieved. From the results in reference [1] the range of the initial molar ratio of $C^0_{H_2O_2}$ to C^0_{2-CP} (R), was varied from 0 to 50 (four levels); the catalyst loading was varied in four levels from 0 to 2 g L^{-1} and the temperature was set at 25 °C. Irradiation was varied in three levels, 0, 48 and 100% referred to the maximum power input. All the irradiation levels were measured with actinometry employing potassium ferrioxalate according to the experimental procedure described by Murov et al. [16] and the data interpretation from the work of Zalazar et al. [17] (more information about the reactor, needed to develop the model, can be found in Table 2).

2.5. Preliminary explorations

Blank runs were made to exclude other parallel reaction mechanisms. Thermal non-catalyzed reaction, direct photolysis, and/or direct H_2O_2 oxidation did not change the 2-CP concentration after 6 h of processing time. Running 2-CP solutions with the maximum goethite loading at 25 °C, no changes were found in concentrations before and after the addition of the catalyst. It was considered that there is no loss of pollutant by adsorption. More details may be found in [1].

3. The reaction scheme

A rigorous reaction scheme, feasible for representing the reaction behavior within the range of explored variables, has been presented by Ortiz de la Plata et al. [1] for the usually called heterogeneous Fenton Reaction. In this section, only a very succinct description of it will be exposed. The complete information is shown in Table 3. The reaction, according to this proposal is conceived as the systematic connection of the following clearly differentiated parts: (I) one group of four heterogeneous surface reactions, one of them having manifestly negative effects for the process and (II) two groups of homogeneous reactions, one of them exclusively characteristic of quinone derivatives that are byproducts of 2-CP degradation. Finally, there is a third group of equations derived from the application of radiation in the UVA plus part of the visible radiation, which leads to the Heterogeneous photo-Fenton reaction.

3.1. Heterogeneous, surface and/or interfacial reactions on the solid produced by species coming from the liquid phase

3.1.1. Proton induced iron dissolution

The iron species incorporated into the solution is Fe^{3+}. During the first stages of goethite dissolution, this reaction has been found to be directly proportional to the proton concentration [18]; hence, its consequences are exclusively observed at acidic conditions.

3.1.2. Reductive induced iron dissolution by chlorohydroquinone

2-CP degradation produces several quinone byproducts, such as chlorobenzoquinone (ClBQ) and chlorohydroquinone (ClHQ). Some of them, particularly the ClHQ, similarly to the case indicated in Section 3.1.1, can produce iron leaching from goethite according to the mechanistic steps described in [1]. It should be noticed that in this case, the dissolved ion takes the form of Fe^{2+}. The reductive induced dissolution is the most important mechanism for iron solubilization in waters among the different possible alternatives [18]. Its maximum significance has been found experimentally at pH 3–4 [19].

3.1.3. Unproductive destruction of hydrogen peroxide

Let us consider the reaction that is seriously counterproductive to the process. The interaction of hydrogen peroxide with different metal oxides having large surface area is well known. In the case of goethite, reference [12] has shown with a detailed study that the decomposition rate, at low H_2O_2 concentrations, follows simple second order reaction kinetics of the form:

$$\Re_{H_2O_2} = -k\, C_{H_2O_2}\, C_{\triangleright FeOOH} \quad (1)$$

In Eq. (1), $\triangleright$FeOOH represents the bond to the oxihydroxide surface.

They have found that at pH 7 the iron dissolution is undetectable. This is in accordance with the phenomenon that will be discussed in the next section. In our work, the H_2O_2 consumption does not bear any stoichiometric relationship with the 2-CP degradation. From the kinetic point of view, it can be

Table 2
Characteristics of the experimental reactor.

Reactor inner diameter	17 cm
Main characteristic dimension of radiation propagation	Operating depth = 9.0 cm
Reaction liquid volume without solid catalyst	2000 cm^3
For the photo-Fenton reaction	Irradiated from the bottom
Reactor bottom made of two layers to produce diffuse irradiation	(1) UVA transparent poly-methylmethacrylate plate (2) Ground glass (borosilicate)
Lamp for the photo-Fenton Reaction	Tubular, located at the focal axis of a parabolic cylinder reflector
Lamp type	Phillips TL'D 18 W/08
Nominal input power	18 W
Lamp emission	Λ = 340–420 nm (nominal)
Wavelength range	λ = 350–400 nm (actual)
Lamp diameter	2.6 cm
Lamp length	59 cm
Custom made reflector made of aluminum	Polished with a mirror like finish and Alzak™ treatment
Incident radiation at the reactor bottom (100%): from actinometric measurements	5.60×10^{-9} Einstein s^{-1} cm^{-2}

safely considered a parallel reaction with a specific rate constant independently determined, regardless the existing pollutant concentration. However, a very important conclusion of reference [12] is that the second order reaction kinetic expression indicated by Eq. (1), with different specific rate constants, maintains its functional form at different pH values.

3.2. Homogeneous reactions taking place in the bulk of the liquid phase in the absence of radiation

3.2.1. Typical reaction steps of the Fenton reaction

Once very small amounts of iron are dissolved into the liquid phase, which is a *sine qua non* condition for the starting of the *combined homogeneous–heterogeneous* Fenton reaction, one first group of reactions, typical of this process in the homogeneous phase reaction, takes place. Following the classical approach [7], there are seven important reactions that involve the catalytic effect of the cycle $Fe^{3+} \rightleftarrows Fe^{2+}$ when dissolved iron is mixed with H_2O_2 [1].

3.2.2. Additional steps of the Fenton reaction produced by enhancement effects of quinone byproducts

Quinone byproducts can significantly improve the fundamental cycle of the $Fe^{3+} \rightleftarrows Fe^{2+}$ reaction, as it was demonstrated by [13] for aromatic compounds and was shown in [1].

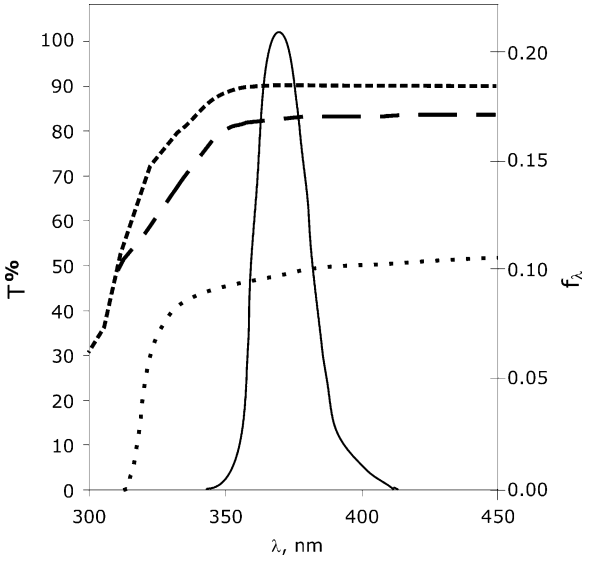

Fig. 2. Left: transmittance of: ———— polymethylmethacrylate, – – – – ground borosilicate glass, ... filter. Right: ———: fraction distribution of wavelength lamp output.

3.3. Reaction enhancement produced by radiation

In this case, there are two additional steps, not considered in reference [1], which lead to a significant increase in the rate of reaction of 2-CP decomposition. They are shown in Table 4 (Steps 20 and 21). These steps are activated by UVA and a large portion of the visible spectrum. Each one of them, define one additional reaction parameter that, in this particular case, are polychromatic primary quantum yields with a value that, from definition, cannot be larger than 1 mol $Einstein^{-1}$. The effect of these steps is shown in Fig. 3. One of them is the well-known generation of $HO^{\bullet}$ radicals from iron coordination complexes. The second is an additional generation of the same radical from ClBQ that increases even further the previously mentioned enhancement effect.

Summarizing, Tables 3 and 4 give the details of the proposed mechanism. The surface reactions are indicated with dark gray shading, whereas light gray shading represents the effects of quinones in either the Fenton (dark) or the photo-Fenton reaction.

4. Kinetics of the heterogeneous Fenton and photo-Fenton reaction

A word of caution with respect to this work is necessary. One part of this kinetic study has a critical problem that shares with the majority of solid catalyzed reactions, but with a larger degree of

Table 3
Proposed reaction scheme.

No. 1	$H_2O_2 \xrightarrow{\triangleright FeOOH} \frac{1}{2}O_2 + H_2O$	[12]
No. 2	$k_2 C_{\triangleright FeOOH}$	[18]
No. 3	$Fe^{3+} + H_2O_2 \rightarrow Fe^{2+} + H^+ + HO_2^{\bullet}$	[7,13]
No. 4	$Fe^{2+} + H_2O_2 \rightarrow Fe^{3+} + HO^- + HO^{\bullet}$	[7,13]
No. 5	$H_2O_2 + HO^{\bullet} \rightarrow HO_2^{\bullet} + H_2O$	[7,13]
No. 6	$H_2O_2 + HO_2^{\bullet} \rightarrow HO^{\bullet} + H_2O + O_2$	[7,13]
No. 7	$Fe^{3+} + HO_2^{\bullet} \rightarrow Fe^{2+} + H^+ + O_2$	[7,13]
No. 8	$Fe^{2+} + HO_2^{\bullet} + H^+ \rightarrow Fe^{3+} + H_2O_2$	[7,13]
No. 9	$Fe^{2+} + HO^{\bullet} \rightarrow Fe^{3+} + HO^-$ + HO	[7,13]
No. 10	$HO^{\bullet}$ + 2-CP → ClDHCD$^{\bullet}$	[13,20]
No. 11	Fe^{3+} + ClDHCD$^{\bullet}$ → Fe^{2+} + ClHQ + H^+	[13,20]
No. 12	$2\{\triangleright FeOOH\} + ClHQ \rightleftarrows 2Fe^{2+} + ClBQ + 2H_2O$	[18,19]
No. 13	Fe^{3+} + ClHQ → Fe^{2+} + ClSQ$^{\bullet}$ + H^+	[13,20]
No. 14	Fe^{3+} + ClSQ$^{\bullet}$ → Fe^{2+} + ClBQ + H^+	[13,20]
No. 15	ClDHCD$^{\bullet}$ + O_2 → ClHQ + $HO_2^{\bullet}$	[13,21]
No. 16	ClDHCD$^{\bullet}$ + O_2 → Other products	[13,21]
No. 17	$HO^{\bullet}$ + ClBQ → Products	[13,20]
No. 18	$HO^{\bullet}$ + ClDHCD$^{\bullet}$ → Products	[13,20]
No. 19	$HO^{\bullet}$ + ClHQ → Products	[13,20]

2-CP: 2-chlorophenol; ClDHCD$^{\bullet}$: chlorodihydroxycyclohexadienyl radical; ClHQ: chlorohydroquinone; ClBQ: chlorobenzoquinonel ClSQ$^{\bullet}$: chlorosemiquinone radical; ▷ Represents a bond to the oxihydroxide surface in the solid goethite.

Table 4
Photo-Fenton additional reaction steps.

No. 20	$Fe^{III}(OH)^{2+} \xrightarrow{h\nu} Fe^{2+} + HO^{\bullet}$	[7]
No. 21	$ClBQ \xrightarrow{h\nu} ClSQ^{\bullet} + HO^{\bullet}$	[13]

Step No. 20. The reaction constant is the polychromatic quantum yield for step 20: $\Phi_{Fe(OH)^{2+}}$ in units of Einstein mol^{-1}. Step No. 21 The reaction constant is the polychromatic quantum yield for step 21: Φ_{ClBQ} in units of Einstein mol^{-1}.

difficulty. Reaction kinetics on a catalyst depends upon all the characteristics of the solid. They may range from its elemental composition, crystalline structure, particle size, specific surface area and pore distribution to the presence of artificially added dopants and all the different forms of the catalyst fabrication. In other words, the kinetic constants may be unique only for a given prepared batch for which all the above-mentioned characteristics are constant. Goethite adds to all these factors the circumstance that very often is prepared from natural oxides having a large variety of very small amounts – sometime traces – of impurities. On occasions, they are prepared from pure oxides but brought to the reported size, using different types of binders. Hence, the validity of the kinetic constants for the surface reactions is limited to the batch of particles that were used to perform the experiments [18].

Accepting the above-mentioned limitations, the problem was solved in three steps as follows: (i) evaluation of the kinetic constant of step No. 1 from experiments made at three different temperatures. This is the only case in which the work departs from the condition of isothermal operation at 25 °C. (ii) Evaluation of the unknown constants of steps Nos. 2 and 10 for the Fenton reaction by parameter estimation, using values for step reactions Nos. 3–9, No. 11 and No. 13–19 within the range of data reported in the literature [7,13,20] and [21]. In some occasions, they had to be used only as very good starting values for the estimation, the reason being that, since they were reported without the confidence interval, the parameter estimator suggested some changes (always within the same order of magnitude). The estimation of the constant for reaction No. 12 was postponed because at 25 °C, the concentration of ClHQ was below the limit of detection of the analytical method (in fact, it was only identified by GCMS measurements). Finally, (iii) Evaluation of the kinetic constants of steps Nos. 12, 20 and 21 using all the data of the Fenton and the photo-Fenton experiments. Under irradiation conditions, the concentration of ClHQ was accurately measured. The general methodology is described in Fig. 4.

All the experiments concerning the heterogeneous Fenton (dark or thermal) reaction have been described and analyzed in [1]. Those corresponding to the photo-Fenton reaction will be explained in the corresponding section (Section 4.3).

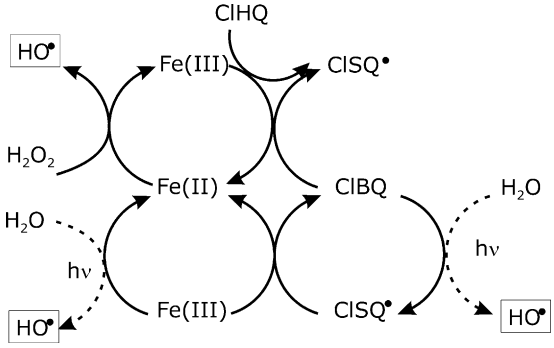

Fig. 3. Schematic representation of irradiation chemical effects.

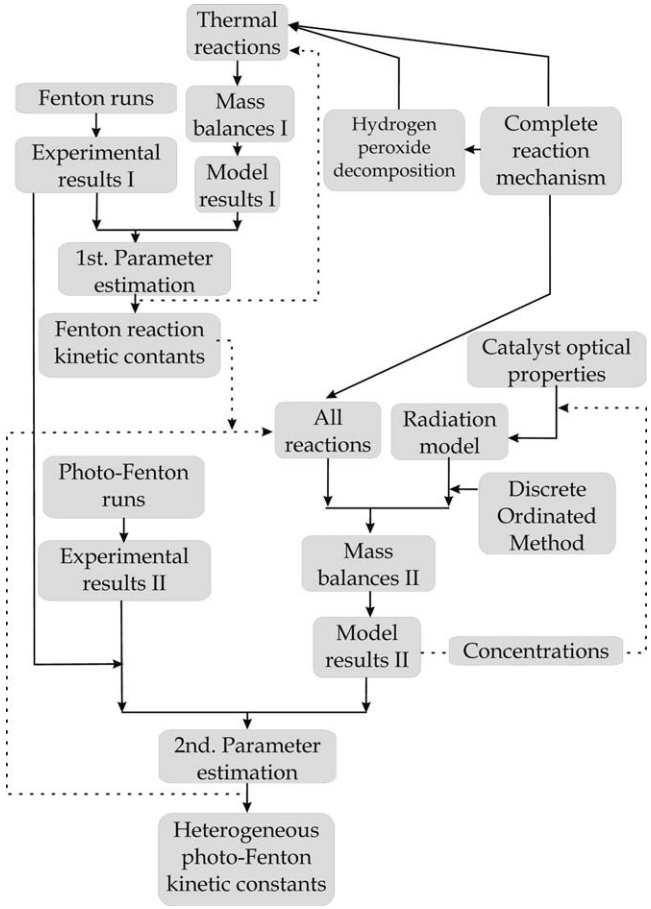

Fig. 4. Flow diagram of parameter's estimation procedure.

4.1. Evaluation of k_1

Lin and Gurol [12] proposed an 11 step mechanism for the decomposition of hydrogen peroxide with goethite. Based on the known information about some of the steps, they were able to obtain a kinetic expression of the form:

$$\Re_{H_2O_2} = -\frac{k^* C_{H_2O_2} C_{\triangleright FeOOH}}{1 + K^* C_{H_2O_2}} \quad (2)$$

In Eq. (2) k^* and K^* are lumped kinetic constants. They also follow the typical Langmuir–Hinshelwood behavior that, at low H_2O_2 concentrations, as the ones used in this work, Eq. (2) reduces to:

$$\Re_{H_2O_2} = -k_1 C_{H_2O_2} C_{\triangleright FeOOH} \quad (3)$$

In the absence of irradiation, eight runs were performed at 25, 37.5 and 50 °C. For an expression of the form: $k_1 = k_0[\exp(-E_a/RT)]$ the following values were obtained: $k_0 = 2.9 \pm 0.14$ cm^2 g^{-1} s^{-1} and $E_a = 49.2 \pm 3.0$ kJ mol^{-1}. At 25 °C, the following kinetic constant was calculated: $k_1 = 6.75 \times 10^{-2}$ cm^2 g^{-1} s^{-1}. The calculated activation energy is an acceptable value according to [22]. It is even more important to compare this value with the one reported by [12] at pH 7 and equal to 32.8 kJ mol^{-1}, when it is known that the decomposition reaction is a very strong function of pH; i.e., at higher pH values a significant increase in the consumption rate takes place [23].

4.2. Evaluation of k_2 and k_{10}

The Fenton reaction in a first stage, will be considered to depend on 18 steps of the mechanism described in Table 3, since as said

Table 5
Reactions rates and kinetic constants.

Step	Reaction	Math. expression	Constant	Units
No. 1	r_1	$k_1 C_{H_2O_2} C_{\triangleright FeOOH}$	6.75×10^{-5}	$g^{-1}\,L\,s^{-1}$
No. 2	r_2	$k_2 C_{\triangleright FeOOH}$	5.28×10^{-11}[a]	$mol\,g^{-1}\,s^{-1}$
No. 3	r_3	$k_3 C_{Fe^{3+}} C_{H_2O_2}$	2.00×10^{-2}	$M^{-1}\,s^{-1}$
No. 4	r_4	$k_4 C_{Fe^{2+}} C_{H_2O_2}$	5.30×10	$M^{-1}\,s^{-1}$
No. 5	r_5	$k_5 C_{H_2O_2} C_{HO^\bullet}$	2.70×10^{7}	$M^{-1}\,s^{-1}$
No. 6	r_6	$k_6 C_{H_2O_2} C_{HO_2^\bullet}$	3.00	$M^{-1}\,s^{-1}$
No. 7	r_7	$k_7 C_{Fe^{3+}} C_{HO_2^\bullet}$	1.00×10^{4}	$M^{-1}\,s^{-1}$
No. 8	r_8	$k_8 C_{Fe^{2+}} C_{HO_2^\bullet}$	1.20×10^{6}	$M^{-1}\,s^{-1}$
No. 9	r_9	$k_9 C_{Fe^{2+}} C_{HO^\bullet}$	3.20×10^{8}	$M^{-1}\,s^{-1}$
No. 10	r_{10}	$k_{10} C_{2CP} C_{OH^\bullet}$	1.31×10^{9}	$M^{-1}\,s^{-1}$
No. 11	r_{11}	$k_{11} C_{Fe^{3+}} C_{ClDHCD^\bullet}$	6.98×10^{3}	$M^{-1}\,s^{-1}$
No. 12	r_{12}	$k_{12} C_{ClHQ} C^2_{\triangleright FeOOH}$	5.28×10^{-6}[a,b]	$g^{-2}\,L^2\,s^{-1}$
No. 13	r_{13}	$k_{13} C_{Fe^{3+}} C_{ClHQ}$	4.40×10^{2}	$M^{-1}\,s^{-1}$
No. 14	r_{14}	$k_{14} C_{Fe^{3+}} C_{ClSQ^\bullet}$	2.20×10^{4}	$M^{-1}\,s^{-1}$
No. 15	r_{15}	$k_{15} C_{ClDHCD^\bullet} C_{O_2}$	6.00×10^{9}[c]	$M^{-1}\,s^{-1}$
No. 16	r_{16}	$k_{16} C_{ClDHCD^\bullet} C_{O_2}$	4.00×10^{9}[c]	$M^{-1}\,s^{-1}$
No. 17	r_{17}	$k_{17} C_{ClBQ} C_{HO^\bullet}$	2.40×10^{9}	$M^{-1}\,s^{-1}$
No. 18	r_{18}	$k_{18} C_{ClDHCD^\bullet} C_{HO^\bullet}$	2.00×10^{10}	$M^{-1}\,s^{-1}$
No. 19	r_{19}	$k_{19} C_{ClHQ} C_{HO^\bullet}$	1.40×10^{10}	$M^{-1}\,s^{-1}$
No. 20	r_{20}	$\bar{\Phi}_{Fe(OH)^{2+}} e^a_{Fe(OH)^{2+}}$	0.159[b]	mol Einstein^{-1}
No. 21	r_{21}	$\bar{\Phi}_{ClBQ} e^a_{ClBQ}$	0.997[b]	mol Einstein^{-1}

[a] C_{H^+} is assumed constant and included in the rate constant.
[b] Computed with parametric estimations made with the entire set of runs.
[c] Oxygen concentration was 0.25 mM.

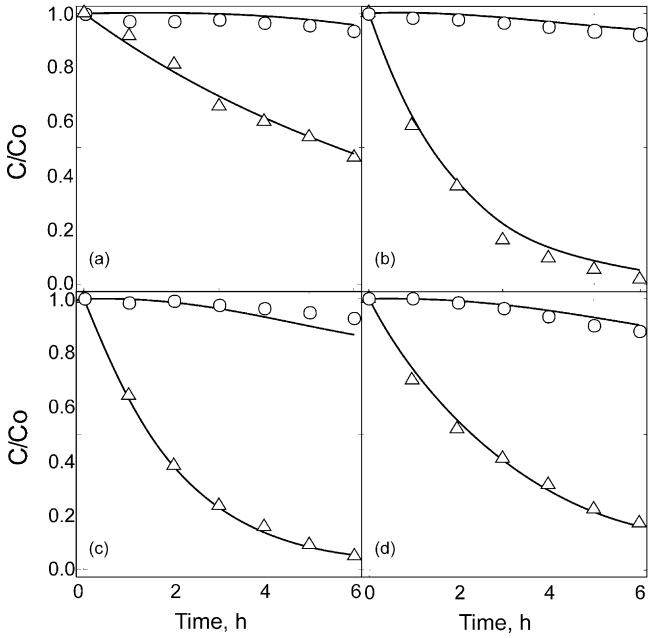

Fig. 5. Heterogeneous Fenton reaction results; solid lines are results from model simulations. ○: 2-CP concentration, Δ: H_2O_2 concentration. T = 25 °C; (a) R = 28.6, $C_{mc,G}$ = 0.5 g L^{-1}; (b) R = 27.5, $C_{mc,G}$ = 2.0 g L^{-1}; (c) R = 51.7, $C_{mc,G}$ = 2.0 g L^{-1}; (d) R = 39.1, $C_{mc,G}$ = 1.25 g L^{-1}.

before, it was not possible to obtain in the dark reaction, and at 25 °C, accurate values of the ClHQ concentration. The reacting system has 10 different species. It is possible to write a mass balance in terms of the mass action law as it is shown for each step in Table 5. Then, a set of 10 ordinary differential equations (ODE) can be defined as they are described in Table 6 based on the previous detailed report. During this part of the work, in a first approximation, the maximum observed total iron concentration of 0.15 ppm was used. This approach does not invalidate the obtained results because all the kinetic constants will be calculated again with the irradiated reaction, employing the entire 21 steps, under conditions where the iron and ClHQ concentrations were accurately measured.

The model simulations concentration results for the 18 steps were compared with the experimental runs at 25 °C described in [1] employing a non-linear, multi-parameter estimator that incorporated an optimization program based on the Levenberg–Marquardt algorithm [24,25]. The model simulations, compared with the experimental results are shown in Fig. 5(a–d) for a wide diversity of experimental conditions. The agreement is very satisfactory. In spite of it, a better test will be obtained if the obtained values, particularly, k_2 and k_{10}, are ratified with the experiments performed employing radiation. In any event, it should be noted that working at 25 °C, regardless the catalyst loading and the hydrogen peroxide concentration, the degradation of 2-CP is unsatisfactory. It is clear that under these operating conditions the process is ineffective and that as shown in reference [1] the problem is only partially solved at 50 °C and with the catalyst concentration significantly reduced.

Table 6
System of ODE for the Fenton reactions.

Mass balances in the well-mixed batch reactor	
$\frac{dC_{H_2O_2}}{dt} = -r_1 - r_3 - r_4 - r_5 - r_6 + r_8$	(4)
$\frac{dC_{Fe^{3+}}}{dt} = r_2 - r_3 + r_4 - r_7 + r_8 + r_9 - r_{11} - r_{13} - r_{14}$	(5)
$\frac{dC_{Fe^{2+}}}{dt} = r_3 - r_4 + r_7 - r_8 - r_9 + r_{11} + r_{13} + r_{14}$	(6)
$\frac{dC_{HO^\bullet}}{dt} = r_4 - r_5 + r_6 - r_9 - r_{10} - r_{17} - r_{18} - r_{19}$	(7)
$\frac{dC_{HO_2^\bullet}}{dt} = r_3 + r_5 - r_6 - r_7 - r_8 + r_{15}$	(8)
$\frac{dC_{2\text{-}CP}}{dt} = -r_{10}$	(9)
$\frac{dC_{ClDHCD^\bullet}}{dt} = r_{10} - r_{11} - r_{15} - r_{16} - r_{18}$	(10)
$\frac{dC_{ClHQ}}{dt} = r_{11} - r_{13} + r_{15} - r_{19}$	(11)
$\frac{dC_{ClSQ^\bullet}}{dt} = r_{13} - r_{14}$	(12)
$\frac{dC_{ClBQ}}{dt} = r_{14} - r_{17}$	(13)

Initial conditions: $t = 0 \rightarrow C_{H_2O_2} = C^0_{H_2O_2}$; $t = 0 \rightarrow C_{2\text{-}CP} = C^0_{2\text{-}CP}$; for all other species: $C_i = 0$.

4.3. Experimental results employing radiation

In the final part of this study described in this section, all the runs made with the Heterogeneous Fenton (dark) reaction described in reference [1] and the new ones made with radiation, were used. The results obtained with illumination are briefly discussed in this section.

A typical selection is shown in Table 7. In this Table, with comparison purposes, two runs of the Fenton reaction made at 25 °C are also included (R1T F and R5T F). It should be noted that with the employed radiation wavelength, the possibility of direct degradation produced by direct photolysis or H_2O_2 + UV can be safely disregarded. Hence, from these results it can be immediately concluded that at 25 °C, the enhancement produced by UVA radiation is very important. As shown in Fig. 6, with 2 g L^{-1} of goethite, R = 53 and 100% irradiation, after 6 h of operation, $X_{2\text{-}CP}$ conversion is 88.5% versus 19.1% with the Fenton reaction; TOC conversion is 73.1% versus 10.0% and hydrogen peroxide consumption is 90.6% versus 94.7% respectively. Improvement is very significant in spite of the fact that reaction times are still too long and hydrogen peroxide consumption remains very high. In these results, it should also be noted that quantification of ClHQ by HPLC has been possible. An additional important point is the very low iron concentration in the solution that was required to carry out the reaction.

These results are valid to make a verification of the proposed model, but at the same time, they indicate the necessity of a very

Table 7
Typical results employing radiation ($T = 25\,^{\circ}C$).

	$C_{cat.}$ ($g\,L^{-1}$)	$R = \frac{C_{H_2O_2}}{C_{2\text{-}CP}}$	Radiation (%)	$X_{2\text{-}CP}$ (%)	X_{TOC} (%)	$X_{H_2O_2}$ (%)	$C_{Fe^{2+}}$ (ppm)[a]	$C_{Fe^{3+}}$ (ppm)[a]
R1T F	2	50	0	19.1	10.0	94.7	–	–
R5T F	0.5	50	0	7.3	6.9	47.4	–	–
R1T P-F	2	53.4	100	88.5	73.1	90.6	0.017	0.291
R2T P-F	2	29.1	100	62.7	46.4	95.6	0.033	0.237
R3T P-F	0.5	48.9	100	41.5	21.1	43.0	0.002	0.048
R4T P-F	0.5	30	100	41.4	20.0	45.0	0.003	0.048
R5T P-F	1.25	39.9	47	53.9	37.7	83.2	0.008	0.151
R6T P-F	1.25	26.2	100	86.6	59.9	84.4	0.012	0.156
R7T P-F	1.25	39.5	100	88.6	58.5	79.7	0.008	0.164
R8R P-F	1.25	39.9	47	52.1	33.5	81.4	0.008	0.159

[a] In this Table, $C_{Fe^{2+}}$ and $C_{Fe^{3+}}$ were calculated from simulation results.

important optimization of the operating conditions to make this process practicable.

Table 5 adds two more reactions to the proposed model in Table 4. The first one is the result of the formation of iron coordination complexes with hydroxyl ions of different nature. According to Pignatello et al. [7] for values of pH in the order of 3 the main existing complexes are formed by $Fe^{(III)}$ with the structure of $Fe^{(III)}(OH)^{2+}$ and $Fe_2^{(III)}(OH)_2^{4+}$. Either compound absorbs both UVA and visible radiation. It is known that under the stated operating condition the most preponderant compound is the first one, with the additional dominance of a larger absorption coefficient. Upon absorption of light, $Fe^{(III)}(OH)^{2+}$ decomposes giving rise to reaction step 20. The result is a significant increase in the generation rate of $HO^{\bullet}$ radicals and simultaneously rebuilt of the Fe^{2+} concentration, which is one of the slowest steps in the thermal Fenton reaction. The optimum pH is in the range of $2.5 < pH < 3$–4 because in this span, the most convenient complex reaches the larger proportion and, at the same time the iron remains always in solution. One could conclude that under the selected pH of this work, these conditions are fulfilled.

In our experimental results, it was already mentioned that the formation of ClHQ was much more significant; this phenomenon occurred without a parallel equivalent increase in ClBQ formation. The existence of this observable response and its contribution to the homogeneous photo-Fenton reaction in the presence of phenolic compounds was exhaustibly described in reference [13]. The reaction was incorporated in Table 4. It is important to note that in real terms, this reaction implies the equivalent to the formation of two additional $HO^{\bullet}$ radicals because the generation of the $ClHQ^{\bullet}$ radical immediately leads to the formation of Fe^{2+} according to reaction step No. 14. The possibility of occurrence of this reaction in the system under study will be even clearer with the discussion that follows below.

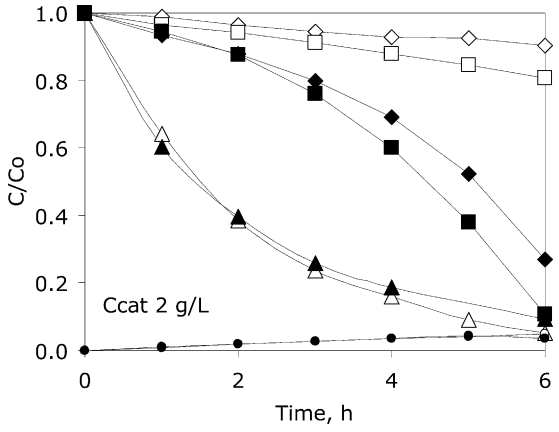

Fig. 6. Experimental results. White symbols: heterogeneous Fenton results; black symbols: heterogeneous photo-Fenton results. ◇: TOC concentration; □: 2-CP concentration; △: H_2O_2 concentration; ○: iron concentrations.

4.4. Evaluation of k_{12}, $\bar{\Phi}_{Fe(OH)^{2+}}$ and $\bar{\Phi}_{\lambda,ClBQ}$

The confirmation of the previously obtained kinetic constants and the need to calculate the new ones (k_{12}, $\bar{\Phi}_{Fe(OH)^{2+}}$, $\bar{\Phi}_{ClBQ}$), makes necessary to reformulate the mass balance $\bar{\Phi}_{Fe(OH)^{2+}}$ is the polychromatic, wavelength averaged, primary reaction quantum yield for step 20 and $\bar{\Phi}_{ClBQ}$ is the polychromatic, wavelength average, primary reaction quantum yield for step 21. The resulting modifications in the set of ODE are shown in Table 8. It is clear that every time that reactions r_{20} and r_{21} must be calculated, a precise description of the radiation field is needed.

These reactions are the result of absorption of light by the corresponding reactant and the local value of each of them is formulated in terms of the product of the respective monochromatic primary[1] quantum yield and the monochromatic local volumetric rate of photon absorption by the said reactant [the LVRPA, $e^a_\lambda(x,t)$] and integrated over the entire wavelength range of interest:

$$r_{20} = \int_{\lambda=350}^{\lambda=400} \Phi_{\lambda,Fe(OH)^{2+}} e^a_{\lambda,Fe(OH)^{2+}}(x,t)\,d\lambda \tag{20}$$

$$r_{21} = \int_{\lambda=350}^{\lambda=400} \Phi_{\lambda,ClBQ} e^a_{\lambda,ClBQ}(x,t)\,d\lambda \tag{21}$$

In order to calculate each of the LVRPA needed for Eqs. (20) and (21) it is necessary to know the spatial distribution of the radiation field which is, by its own nature, irreducible non-uniform. As it will be pointed out below, to calculate the polychromatic value of $e^a_\lambda(x,t)$ for each radiation absorbing species, it will be necessary to know all the optical properties of the system as well as the detailed characteristics of the radiation source.

4.4.1. Mathematical description of the radiation field

The model for the radiation field comprises three steps: (i) To formulate the radiation balance or – more properly denominated – the radiative transfer equation (RTE) for a heterogeneous system. (ii) To measure or to gather from the literature the data of the optical properties of the participating species in the reaction that are needed to compute the RTE and (iii) to determine the boundary condition for solving the RTE. With all this information, the radiation field can be obtained by numerical integration of the RTE. Afterwards, it will be necessary to propose an approximation for the polychromatic quantum yield for reactions steps (20) and (21).

[1] Primary quantum yields are precisely defined only for monochromatic radiation.

Table 8
Modified system of ODE for the photo-Fenton reactions.

Modifications in the mass balances in the well-mixed batch reactor	
$\frac{dC_{Fe^{3+}}}{dt} = r_2 - r_3 + r_4 - r_7 + r_8 + r_9 - r_{11} - r_{13} - r_{14} - r_{20}$	(14)
$\frac{dC_{Fe^{2+}}}{dt} = r_3 - r_4 + r_7 - r_8 - r_9 + r_{11} + 2r_{12} + r_{13} + r_{14} + r_{20}$	(15)
$\frac{dC_{HO^{\cdot}}}{dt} = r_4 - r_5 + r_6 - r_9 - r_{10} - r_{17} - r_{18} - r_{19} + r_{20} + r_{21}$	(16)
$\frac{dC_{ClHQ}}{dt} = r_{11} - r_{12} - r_{13} + r_{15} - r_{19}$	(17)
$\frac{EC_{ClSQ^{\cdot}}}{dt} = r_{13} - r_{14} + r_{21}$	(18)
$\frac{dC_{ClBQ}}{dt} = r_{12} + r_{14} - r_{17} - r_{21}$	(19)

Eqs. (4), (8), (9) and (10) from Table 6, remain unchanged. Initial conditions: $t = 0 \rightarrow C_{H_2O_2} = C^0_{H_2O_2}$; $t = 0 \rightarrow C_{2\text{-CP}} = C^0_{2\text{-CP}}$; for all other species: $C_i = 0$.

4.4.1.1. The formulation of the RTE. Under isothermal conditions, the only remaining term of the thermal energy equation is the radiation contribution. This reaction is performed in a radiation transport, heterogeneous participating medium. The complete RTE considering absorption and scattering must be used. Working at low temperatures, radiation emission can be neglected. Let us assume for the moment that the spectral, linear volumetric absorption coefficients $\sum_i \kappa_{\lambda,i}(\underline{x}, y)$ are known for all the "*i*" species in the solution. Consider also, as indicated in Section 2.2, that the spectral, specific volumetric absorption $[\kappa^*_{\lambda,G}]$ and scattering $[\sigma^*_{\lambda,G}]$ coefficients of goethite, as well as the corresponding phase function (p_λ) for scattering is also known (the Henyey and Greenstein model [14]). In addition, assume for the moment, that the molar absorption coefficients of all the intervening species in the solution are also available. Then, for a single wavelength λ and a single direction of propagation (expressed in a spherical coordinate system) $\underline{\Omega}(\theta, \phi)$, it is possible to write [26]:

$$\frac{dI_{\underline{\Omega},\lambda}}{ds}(s,t) + \underbrace{\kappa^{Tot.}_\lambda(s,t)\ I_{\underline{\Omega},\lambda}(s,t)}_{\text{Absorption}} + \underbrace{\sigma_\lambda(s,t)\, I_{\underline{\Omega},\lambda}(s,t)}_{\text{Out-scattering}} = \underbrace{\frac{\sigma_\lambda(s,t)}{4\pi} \int_{\Omega'=4\pi} p_\lambda(\underline{\Omega}' \rightarrow \underline{\Omega}) I_{\underline{\Omega},\lambda}(s,t)\, d\Omega'}_{\text{In-scattering}} \quad (22)$$

where s is a directional coordinate in a three-dimensional space and $\underline{\Omega}$ is a unit vector indicating the propagating direction of this particular radiation beam. $\underline{\Omega}'$ indicates all other directions of propagation that contribute to direction $\underline{\Omega}$ due to in-scattering. The phase function for scattering is:

$$p_{HG,\lambda}(\mu_0) = \frac{1 - g^2_\lambda}{(1 + g^2_\lambda - 2g_\lambda \mu_0)^{3/2}} \quad (23)$$

Here, μ_0 is the cosine of the exiting angle between directions $\underline{\Omega}'$ and $\underline{\Omega}$. Values of g_λ are given in Table 1.

At this point, it is necessary to recall that for the equipment described in Fig. 1, with proper consideration of well-defined geometrical dimensions and configurations, the reactor can be modeled as one-dimensional system [27]. With the inclusion of the ground glass bottom (see Section 2.4), the entering diffuse radiation permits to assume azimuthal symmetry and work with a one-directional RTE. Then Eq. (22) can be written employing the one-dimensional–one-directional model [28] as:

$$\mu \frac{\partial I_\lambda(x,t,\mu)}{\partial x} + \kappa^{Tot.}_\lambda(t)_\lambda I_\lambda(x,t,\mu) + \sigma_\lambda = \frac{\sigma_\lambda}{2} \int_{\mu'=-1}^{1} I_\lambda(x,t,\mu')\, p(\mu' \rightarrow \mu)\, d\mu' \quad (24)$$

As shown in Fig. 7, having a diffuse, isotropic radiation entrance, the produced azimuthal symmetry in the boundary condition, permits to reduce one of the directions of propagation. In Eq. (24)

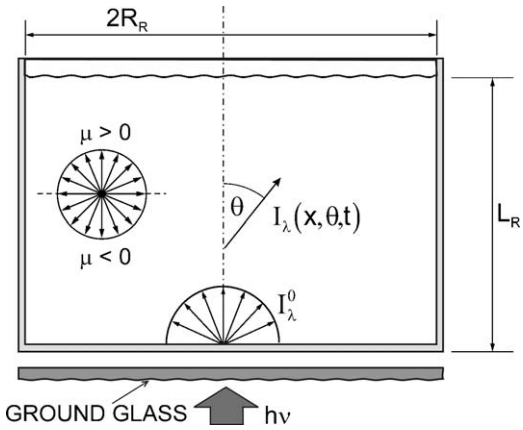

Fig. 7. Representation of the one-dimensional–one-directional radiation model.

$\mu = \cos\theta$. Considering the low scattering produced by the goethite particles and the free surface existing in $x = L_R$, the boundary conditions may be simplified to:

$$x = 0; \quad (\mu > 0) \rightarrow I_\lambda(x,\theta) = I^0_\lambda \neq f(\theta) \quad (25)$$

$$x = L_R; \quad (\mu < 0) \rightarrow I_\lambda(x,\theta) = 0 \quad \text{(no reflection)} \quad (26)$$

This equation can be numerically solved with the Discrete Ordinate Method [29] to obtain the value of I_λ as a function of x, θ and t. Once the value of $I_\lambda(x,t,\mu)$ is known, the LVRPA can be calculated as indicated below.

First, it is necessary to compute the local value of the Incident Radiation at a given point in space, considering all the incoming rays to that point [26]:

$$G_\lambda(x,t) = \int_{\Omega=4\pi} I_\lambda[x,t,\Omega(\theta,\phi)]\, d\Omega \quad (27)$$

With azimuthal symmetry [28]:

$$G_\lambda(x,t) = 2\pi \int_{\mu=-1}^{\mu=1} I_\lambda[x,t,\mu]\, d\mu \quad (28)$$

The Local Volumetric Rate of Photon Absorption (the LVRPA) at each point is the product of the Incident Radiation at that point, times the local value of the respective linear absorption coefficient:

$$e^a_{\lambda,i}(x,t) = \kappa_{\lambda,i}(t) G_\lambda(x,t) = \kappa_{\lambda,i}(t) \left[2\pi \int_{\mu=-1}^{\mu=1} I_\lambda(x,t,\mu)\, d\mu \right] \quad (29)$$

Note that the computation of the spectral specific intensity involves the knowledge of the total absorption coefficient originated by all the species existing in the reaction space (reactants, products, catalyst, inert compounds, etc.); whereas the value of $e^a_{\lambda,i}(x,t)$ employs, exclusively, the linear absorption coefficient of the species under consideration. Thus, to apply the method it is necessary to know the values of all the linear absorption coefficients of the species $[\kappa_{\lambda,i}(t)]$, the linear total absorption coefficient $[\kappa^{Tot.}_\lambda(x,t)]$ and the boundary condition at $x = 0$, I^0_λ.

4.4.1.2. The total, the active species in the homogeneous solution and the solid catalyst absorption coefficients. It is important noting the existence of three types of absorption coefficients: (i) the linear, molar ones corresponding to each type of chemically active species in solution [$Fe^{(III)}(OH)^{2+}$ and CIBQ], (ii) the linear, mass" absorption coefficient pertaining to the solid goethite and (iii) those resulting from any other possible absorbing substances that could produce an inner filtering effect. In this case, only the first two are present.

Using the Beer's approximation, the linear, molar absorption coefficient for the first two can be written as:

$$\kappa_{\lambda,i,\text{Active Solution}}(t) = \begin{cases} \kappa_{\lambda,\text{Fe(OH)}^{2+}} & = \alpha_{\lambda,\text{Fe(OH)}^{2+}} C_{\text{Fe(OH)}^{2+}}(t) \\ \kappa_{\lambda,\text{ClBQ}} & = \alpha_{\lambda,\text{ClBQ}} C_{\text{ClBQ}}(t) \end{cases} \quad (30)$$

Both are defined in terms of molar concentrations. As written in Eq. (30), for a well-stirred reaction space, both are only a function of time.

For the catalyst, it is necessary to define a linear, mass absorption coefficient in terms of mass concentrations:

$$\kappa_{\lambda,\text{mc,G}} = \kappa^*_{\lambda,\text{mc,G}} C_{\text{mc,G}} \quad (31)$$

In Eq. (31) $C_{\text{mc,G}}$ indicates a concentration of goethite in terms of g cm^{-3} (or g L^{-1}) and $\kappa^*_{\lambda,\text{mc,G}}$ is a specific mass absorption coefficient in terms of cm^2 g^{-1} (or 10^3 cm^2 g^{-1}). Here it is safely assumed that the catalyst does not suffer significant changes with time either in its size or in its chemical activity.

Each one of the molar (napierian) absorption coefficients must be known in order to calculate their respective LVRPA. The same is valid for the catalyst.

Besides, the "total" linear napierian absorption coefficient $\kappa_{\lambda,\text{Tot}}(t)$ links the local radiation field to the concentration field of all energy-absorbing species, whether they are chemically active or not. The expression of $\kappa_{\lambda,\text{Tot}}(t)$ is:

$$\kappa_{\lambda,\text{Tot.}}(t) = \sum_k \kappa_{\lambda,k}(\underline{x},t) = \left[\sum_{j,\text{Absorbing Solution}} \alpha_{\lambda,j} C_j(t)\right] + \kappa^*_{\lambda,\text{mc,G}} C_{\text{mc,G}} \quad (32)$$

In Eq. (32), the subscript k extends over all the radiation absorbing species; the summation index j covers all radiation-absorbing species in the homogeneous phase, i.e., excluding the catalyst. The subscript "Absorbing Solution" indicates the absorption coefficient of all the absorbing species in the homogeneous phase. The last term employs mass concentration properties. In our particular case, since the only absorbing species are the "Active Solution" species (because the presence of inner filtering substances is not considered) $j = i = \text{Fe(OH)}^{2+}$ and ClBQ. Table 9 provides useful information for our calculations considering the following special case: (1) the employed iron concentration corresponds to the maximum one measured in the entire work. (2) Similarly, the employed ClBQ concentration corresponds to an equivalent condition (it should be clear that they do not correspond to the same experimental run). From this Table it can be concluded that as far as the radiation field is concerned, it is almost entirely determined by the absorption produced by goethite that, in addition, adds scattering effects. Even if one counts that all the iron is present as $\text{Fe(OH)}^{2+}$and uses the minimum catalyst concentration, the error would be always below 10%. This means that, as long as the goethite concentration remains constant and its chemical activity unchanged, the existing radiation field can be safely considered independent of time. Thus in Eq. (24) it is safe to write $\kappa_{\lambda,\text{Tot.}} \cong \kappa_{\lambda,\text{cm,G}}$. However, for the kinetics of step reactions (20) and (21), absorption by their respective active components are the ones to take into account.

4.4.1.3. The boundary condition. The boundary condition was calculated with actinometry employing the well-known potassium ferrioxalate reaction [16]. However, the existence of the ground glass plate at the surface of radiation entrance requires a special analysis. In addition, it must be noticed that this analysis requires the inlet boundary condition as a function of wavelength, as it will be seen in what follows.

The actinometric reaction is performed in a perfectly mixed batch reactor; consequently, the mass balance is:

$$\underbrace{\frac{dC_{Fe^{2+}}(t)}{dt}}_{\text{Polychromatic}} = \langle R^{\text{Act.}}_{\sum_\lambda}(x,t)\rangle_{L_R} = \sum_\lambda [\phi^{\text{Act.}}_\lambda \langle e^{\text{a}}_\lambda(x,t)\rangle_{L_R}] \quad (33)$$

In Eq. (33), the integral over the entire wavelength range has been approximated by a summation operation. Values of $\phi_{\lambda,\text{Act.}}$ (the overall quantum yields for the actinometer) are known as a function of wavelength [16]. From Eq. (33) as it is briefly shown in Appendix A:

$$\langle e^{\text{a}}_{\lambda,\text{Act.}}(x,t)\rangle_{L_R} \cong \frac{\kappa_{\lambda,Fe^{3+}} \pi I^0_\lambda}{\kappa_{\lambda,\text{Tot.}} L_R} \quad (34)$$

In Eq. (34) the symbol $\langle [\![\cdot]\!] \rangle_{L_R} = (1/L_R)\int_0^{L_r} [\![\cdot]\!] dx$, stands for an averaging integral of a spatially dependent property $[\![\cdot]\!]$, taken over the reaction space, which for the one-dimensional model extends only over the reactor length.

For the diffuse, isotropic incoming radiation [28]:

$$I^0_\lambda = \frac{G_{\lambda,W}}{2\pi} \quad (35)$$

where $G_{\lambda,W}$ is the incident radiation on the surface of the reactor bottom. Substituting Eqs. (34) and (35) into Eq. (33) and considering polychromatic radiation, the result is:

$$\langle R^{\text{Act.}}_{\sum_\lambda}(x,t)\rangle_{L_R} = \sum_\lambda \left[\phi_{\lambda,\text{Act.}} \frac{\kappa_{\lambda,Fe^{3+}} G_{\lambda,W}}{2\kappa_{\lambda,\text{Tot.}} L_R}\right] = \underbrace{\frac{dC_{Fe^{2+}}(t)}{dt}}_{\text{Polychromatic}} \quad (36)$$

Working with low conversions as recommended, $\kappa_{\lambda,\text{Tot.}} = \kappa_{\lambda,Fe^{3+}} + \kappa_{\lambda,Fe^{2+}} \cong \kappa_{\lambda,Fe^{3+}}$.

In order to know the wavelength distribution of the incoming radiation, the said distribution of the lamp output (Fig. 2) f_λ (expressed in W) must be transformed into a distribution in terms of Einstein s^{-1} ($f_{\lambda,E}$). It is assumed that this distribution is maintained at $x = 0$, then;

$$G_{\lambda,W} = f_{\lambda,E} G_{W,\text{Tot.}} \quad (37)$$

Table 9
Molar, linear molar and linear mass absorption coefficients.

λ (nm)	$\alpha^*_{\lambda,\text{Fe(OH)}^{2+}}$ [a] (cm^2 mol^{-1})	$\kappa_{\lambda,\text{Fe(OH)}^{2+}}$ [b] (cm^{-1})	$\alpha^*_{\lambda,\text{ClBQ}}$ [c] (cm^2 mol^{-1})	$\kappa_{\lambda,\text{ClBQ}}$ [d] (cm^{-1})	$\kappa_{\lambda,\text{mc,G}}$ 0.5 g L^{-1} cm^{-1}	$\kappa_{\lambda,\text{mc,G}}$ 1.25 g L^{-1} cm^{-1}	$\kappa_{\lambda,\text{mc,G}}$ 2.0 g L^{-1} cm^{-1}
350	1,289,680	0.0066	1,159,156	0.0214	0.049	0.121	0.194
360	817,565	0.0042	824,410	0.0153	0.054	0.134	0.214
370	483,630	0.0025	505,655	0.0094	0.058	0.144	0.230
380	276,360	0.0014	291,023	0.0054	0.058	0.144	0.230
390	149,695	0.0008	188,957	0.0035	0.054	0.135	0.216
400	80,605	0.0004	147,905	0.0027	0.051	0.128	0.204

[a] Extracted from [33].
[b] Calculated with the maximum concentration of iron in the solution.
[c] Measured in this work (Cary 100 Bio).
[d] Calculated with the maximum concentration of ClBQ in the solution.

Hence, measuring initial reaction rates, as shown in Appendix B, the value of I^0_λ is readily obtained:

$$I^0_\lambda = \frac{L_R f_{\lambda,E}}{\pi \bar{\Phi}_{Act.}} \left\{ \lim_{t\to 0} \frac{\Delta C_{Fe^{+2}}}{\Delta t} \right\} \quad (38)$$

Eq. (38) is the required monochromatic boundary condition for Eq. (24).

4.4.1.4. Evaluation of two photochemical step reactions. Now, let us go back to Eqs. (20) and (21). The parameter estimation procedure will give the values of $\bar{\Phi}_{Fe(OH)^{2+}}$ and $\bar{\Phi}_{ClBQ}$. To calculate $e^a_{\lambda,Fe(OH)^{2+}}(x,t)$ and $e^a_{\lambda,ClBQ}(x,t)$ we have all the required information. To solve Eq. (24) we have the phase function [Eq. (23)], the total linear absorption coefficient [Eq. (34)] and the boundary condition [Eq. (25) = Eq. (38)]. Thus, it is possible to know $I_\lambda(x,t)$. With this value, applying Eqs. (29) and (30), it is possible to have all the results for calculating point and monochromatic values of the LVRPA. Thus, two integrations are necessary: one for the average over the reaction volume and a second one for the employed wavelength interval:

$$a \int_{\lambda=350}^{\lambda=400} \langle r_{i,Active\ Solution} \rangle_{L_R} d\lambda = \int_{\lambda=350}^{\lambda=400} \frac{1}{L_R} \int_{x=0}^{x=L_r} r_{i,Active\ Solution}\, dx\, d\lambda \quad (39)$$

$$\int_{\lambda=350}^{\lambda=400} \frac{1}{L_R} \int_{x=0}^{x=L_r} \langle r_{i,Active\ Solution} \rangle_{L_R} dx\, d\lambda = \int_{\lambda=350}^{\lambda=400} \frac{1}{L_R} \int_{x=0}^{x=L_r} \Phi_{\lambda,i,Active\ Solution} e^a_{\lambda,i,Active\ Solution}(x,t)\, dx\, d\lambda \quad (40)$$

Working with polychromatic light, the monochromatic $\Phi_{\lambda,i,Active\ Solution}$ will not be discriminated by the parameter estimation. Then, an average polychromatic, primary quantum yield was defined in the following way:

$$\bar{\Phi}_{i,Active\ Solution} = \frac{\int_{\lambda=350}^{\lambda=400} \Phi_{\lambda,i,Active\ Solution} e^a_{\lambda,i,Active\ Solution} d\lambda}{\int_{\lambda=350}^{\lambda=400} e^a_{\lambda,i,Active\ Solution} d\lambda} \quad (41)$$

In this average, the weighting factor is the known monochromatic LVRPA for each of the respective species. Then the final equations for the rates are:

$$\int_{\lambda=350}^{\lambda=400} \frac{1}{L_R} \int_{x=0}^{x=L_r} r_{Fe(OH)^{2+}}\, dx\, d\lambda = \frac{1}{L_R} \bar{\Phi}_{Fe(OH)^{2+}} \int_{\lambda=350}^{\lambda=400} \int_{x=0}^{x=L_r} e^a_{\lambda,Fe(OH)^{2+}}(x,t) dx\, d\lambda \quad (42)$$

$$\int_{\lambda=350}^{\lambda=400} \frac{1}{L_R} \int_{x=0}^{x=L_r} r_{ClBQ}\, dx\, d\lambda = \frac{1}{L_R} \bar{\Phi}_{ClBQ} \int_{\lambda=350}^{\lambda=400} \int_{x=0}^{x=L_r} e^a_{\lambda,ClBQ}(x,t)\, dx\, d\lambda \quad (43)$$

4.4.2. Kinetic constants evaluation

Employing all the experimental results of the Fenton and photo-Fenton reactions, the results of the simulation model represented by the modified system of ten ODE, a new parameter estimation was performed employing the previously mentioned non-linear multi-parameter estimator coupled with the Levenberg–Marquardt algorithm [24,25]. The result is a complete set of compatible kinetic constants. They are included in Table 5. It must be noted that both active species absorption coefficients are a function of the species concentration and, consequently of time. This aspect, in general, compels one to solve the RTE coupled with the mass balance. This coupling is even more troublesome when the solution of the set of 12 ODE coupled with the RTE must be solved several hundred times in the optimization program. However, the precise approximation previously discussed that makes $\kappa_{\lambda,Tot.} \cong \kappa_{\lambda,cm,G}$ is a great simplification to this part of the optimization program, since in this way, assuming constant properties for the iron oxide, the mass balances and the RTE become uncoupled. As indicated at the beginning of Section 4.4, in this operation the kinetic constant for step 12 was also obtained.

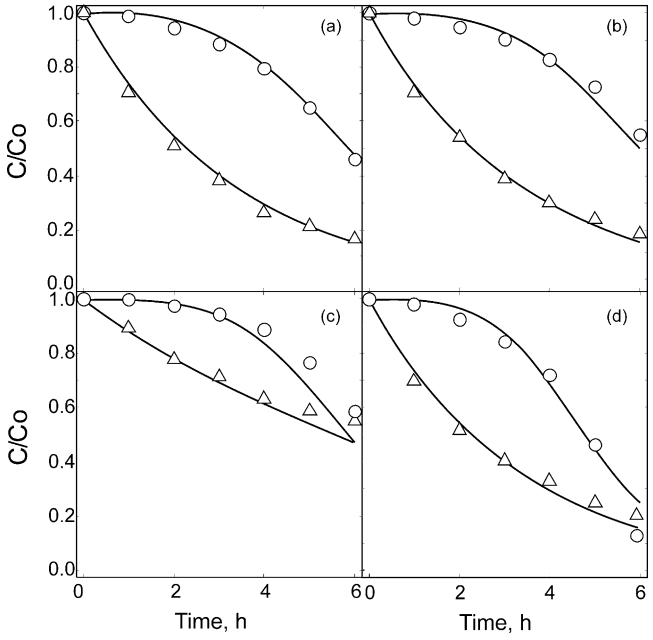

Fig. 8. Heterogeneous photo-Fenton reaction results; solid lines are results from model simulations. ○: 2-CP concentration, Δ: H_2O_2 concentration. T = 25 °C; (a) R = 36.9, $C_{mc,G}$ = 1.25 g L^{-1}, Incident radiation at the reactor bottom: 48%, Fe = 0.168 ppm. (b) R = 39.9, $C_{mc,G}$ = 1.25 g L^{-1}, Incident radiation at the reactor bottom: 48%, Fe = 0.158 ppm. (c) R = 30.0, $C_{mc,G}$ = 0.50 g L^{-1}, Incident radiation at the reactor bottom: 100%, Fe = 0.051 ppm. (d) R = 39.5, $C_{mc,G}$ = 1.25 g L^{-1}, incident radiation at the reactor bottom: 100%, Fe = 0.171 ppm.

4.5. Validation of the results

The obtained results will be validated in three important aspects:

(i) The way in which the radiation model, after the parameter estimation, represents the Heterogeneous photo-Fenton experimental runs under different operating conditions [Fig. 8 (a–d)]. Lines are all results from the model simulation.

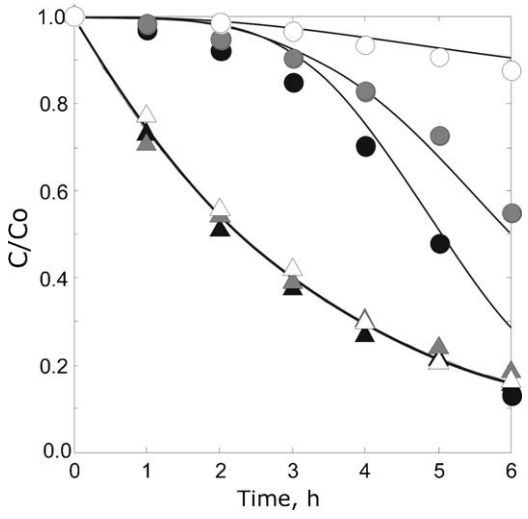

Fig. 9. Effect of incident radiation at the reactor bottom: white symbols 0%; gray symbols 48%; black symbols 100%. ○: 2-CP concentration, Δ: H_2O_2 concentration.

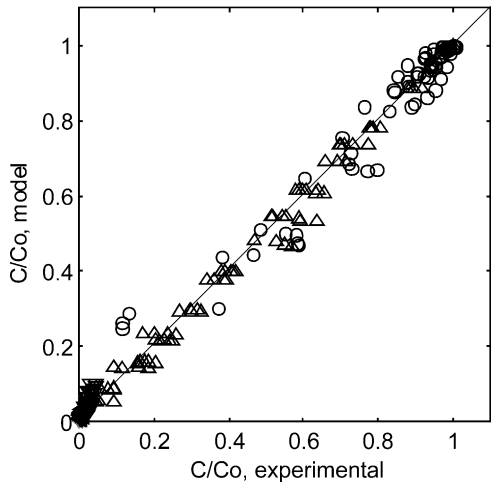

Fig. 10. Graphic representation of the agreement between model simulations and experimental data, including results of Heterogeneous Fenton and photo-Fenton results.

It can be seen that the agreement between simulation results and experimental data is very good.

(ii) The representation of the results corresponding to some typical experimental runs corresponding to the Heterogeneous Fenton and photo-Fenton reaction at different irradiation rates (Fig. 9). Lines are simulation results. Again, the results are very satisfactory. The absence of variations in the hydrogen peroxide concentration is due to its very low linear absorption coefficient in the wavelength range of the employed radiation when it is compared with the one corresponding to goethite. Under this unfavorable competition for the arriving photons, goethite entraps most of them.

(iii) In Fig. 10, a compilation of all the experimental results corresponding to the Heterogeneous Fenton and photo-Fenton reactions is plotted. Here, the ordinate indicates simulation results and the abscissa the corresponding experimental points. At this point it can be said that the model renders a very acceptable representation of the reaction performance.

5. Conclusions

A kinetic study of a proposed combined homogeneous and heterogeneous Fenton and photo-Fenton reactions employing small catalytic particles of goethite as a source of iron to degrade 2-CP has been carried out. The reaction was conducted at pH 3 with a goethite particle size that ensure very fast precipitation after the reaction is completed. Iron dissolution, indispensable for carrying out the homogeneous reaction steps was minimal.

The kinetics was obtained resorting to a feasible reaction scheme, a complete model of the employed photoreactor and a detailed description of the radiation field in the case of the irradiated reactions. The kinetic constants of reaction scheme comprising 21 steps have been obtained. They apply to the heterogeneous–homogeneous Fenton (19 steps) and the Heterogeneous process corresponding to the photo-Fenton reaction (2 additional steps).

The obtained parameters were calculated using 15 values taken from the existing literature that were adopted as such and, in a few cases, used as initializing values for the optimization program. The other six were calculated with the same program, based on models specifically developed or adapted for this work. They include three surface reactions, two photochemical reactions and the interaction of 2-CP with the $HO^{\bullet}$ radical. In both the Fenton and photo-Fenton reactions, the beneficial effects of the presence of quinone byproducts were included.

Reasonable degrees of 2-CP degradation and TOC conversion have been obtained (88.5% and 73.1% respectively) after 6 h of reaction time. However, much work is still needed in order to achieve complete mineralization in practical, shorter reaction times. The obtained results provide the basis for carrying out this subsequent work.

Acknowledgments

The authors would like to thank to Universidad Nacional del Litoral, Consejo Nacional de Investigaciones Científicas y Técnicas and Agencia Nacional de Promoción Científica y Tecnológica for their financial support. The authors gratefully thank Eng. Susana Gervasio for the AAS analysis of the iron samples. The technical assistance of Mr. Antonio Negro and Eng. Claudia Romani are also acknowledged.

Appendix A

An abridged demonstration of the way to calculate $\langle e^{a}_{\lambda,\mathrm{Act.}}(x,t)\rangle_{L_R}$ will be shown here. For more details, the reader can resort to [17,30].

The RTE for a homogeneous medium when the incoming radiation is diffuse is [31]:

$$\mu \frac{\mathrm{d}I_{\lambda,\underline{\Omega}}}{\mathrm{d}x}(x,t) + \kappa_{\lambda,\mathrm{Tot.}}(x,t) I_{\lambda,\underline{\Omega}}(x,t) = 0 \tag{A-1}$$

The boundary condition is I^0_λ. Upon integration:

$$I_{\lambda,\underline{\Omega}}(x,t) = I^0_\lambda \exp\left(-\frac{\kappa_{\lambda,\mathrm{Tot.}} x}{\mu}\right) \tag{A-2}$$

The LVRPA is:

$$e^{a}_{\lambda,\mathrm{Act.}}(x,t) = \kappa_{\lambda,\mathrm{Fe^{3+}}} G_\lambda(x,t) \tag{A-3}$$

Values of $\kappa_{\lambda,\mathrm{Fe^{3+}}}$ and also $\kappa_{\lambda,\mathrm{Fe^{2+}}}$ as a function of wavelength are also known [32].

Calculating the value of $G_{\boldsymbol{\lambda}}(x,t)$ for a homogeneous medium:

$$G_\lambda(x,t) = 2\pi I^0_\lambda \underbrace{\left[\int_0^1 \exp\left(-\frac{\kappa_{\lambda,\mathrm{Tot.}} x}{\mu}\right)\mathrm{d}\mu\right]}_{\text{2nd. order integro exponential function}=E_2} \tag{A-4}$$

After substitution into Eq. (A-3), it must be considered that Eq. (A-4) represents local values, whereas the experimental data correspond to volume-averaged results. Thus, Eq. (A-4) must be integrated. For the one-dimensional model, the averaging integral is performed over L_R:

$$\langle e^{a}_{\lambda,\mathrm{Act.}}\rangle_{L_R} = \frac{1}{L_R}\int_0^{L_r} \kappa_{\lambda,\mathrm{Fe^{3+}}} 2\pi I^0_\lambda E_2(\kappa_{\lambda,\mathrm{Tot.}} x)\,\mathrm{d}x \tag{A-5}$$

For integration, it must be considered that [14,31]:

$$\int E_n(z)\,\mathrm{d}z = -E_{n+1}; \quad E_3(0) = \frac{1}{2}, \quad \text{and} \quad \lim_{z\to\infty} E_3(z) \to 0 \tag{A-6}$$

For the employed actinometer concentrations (0.02 M) and the useful wavelength range (350–400 nm), $\boldsymbol{\kappa}_{\boldsymbol{\lambda}}$,Tol. $L_R \to \infty$. Then, $E_3(x = L_R) \to 0$. Finally:

$$\langle e^{a}_{\lambda,\mathrm{Act.}}(x,t)\rangle_{L_R} \cong \frac{\kappa_{\lambda,\mathrm{Fe^{3+}}} \pi I^0_\lambda}{\kappa_{\lambda,\mathrm{Tot.}} L_R} \tag{A-7}$$

Appendix B

Consider Eq. (33):

$$\underbrace{\frac{dC_{Fe^{2+}}(t)}{dt}}_{\text{Polychromatic}} = \sum_{\lambda}[\phi_{\lambda}^{Act.}\langle e_{\lambda}^{a}(x,t)\rangle_{L_R}] = \sum_{\lambda}\left[\phi_{\lambda}^{Act.}\frac{\kappa_{\lambda,Fe^{3+}}\pi I_{\lambda}^{0}}{\kappa_{\lambda,Tot}L_R}\right] \tag{B-1}$$

At $t \to 0$ (low conversions) $\kappa_{\lambda,Fe^{3+}} \cong \kappa_{\lambda,Tot.}$. Considering Eqs. (35) and (37):

$$\left\{\lim_{t\to 0}\underbrace{\frac{dC_{Fe^{2+}}(t)}{dt}}_{\text{Polychromatic}}\right\} = \frac{1}{2L_R}\sum_{\lambda}\phi_{\lambda,Act.}f_{\lambda,E}G_{W,Tot.} \tag{B-2}$$

Taking into account that $G_{W,Tot.}$ is not a function of λ and resorting again to Eqs. (35) and (37):

$$\left\{\lim_{t\to 0}\underbrace{\frac{dC_{Fe^{2+}}(t)}{dt}}_{\text{Polychromatic}}\right\} = \frac{G_{\lambda,W}}{2L_R f_{\lambda,E}}\sum_{\lambda}\phi_{\lambda,Act.}f_{\lambda,E} = \frac{\pi I_{\lambda}^{0}}{L_R f_{\lambda,E}}\sum_{\lambda}\phi_{\lambda,Act.}f_{\lambda,E} \tag{B-3}$$

From Eq. (B-3):

$$I_{\lambda}^{0} = \frac{L_R f_{\lambda,E}}{\pi\sum_{\lambda}\phi_{\lambda,Act.}f_{\lambda,E}}\left\{\lim_{t\to 0}\underbrace{\frac{dC_{Fe^{2+}}(t)}{dt}}_{\text{Polychromatic}}\right\} \tag{B-4}$$

Defining and average value of the actinometer overall quantum yield:

$$\bar{\Phi}_{Act.} = \sum_{\lambda}\phi_{\lambda,Act.}f_{\lambda,E} \tag{B-5}$$

Under the sated experimental conditions [16,17], at very low conversions, the reaction rate can be safely substituted by the ratio of the incremental values of conversions and times as follows:

$$\underbrace{I_{\lambda}^{0}}_{\text{Monochromatic value}} = \frac{L_R f_{\lambda,E}}{\pi\bar{\Phi}_{Act.}}\left\{\lim_{t\to 0}\underbrace{\frac{\Delta Fe^{2+}}{\Delta t}}_{\text{Polychromatic measurement}}\right\} \tag{B-6}$$

References

[1] G.B. Ortiz de la Plata, O.M. Alfano, A.E. Cassano, Appl. Catal. B: Environ., submitted for publication.
[2] G.B. Ortiz de la Plata, O.M. Alfano, A.E. Cassano, Chem. Eng. J. 137 (2008) 396–410.
[3] A.L. Teel, C.R. Warberg, D.A. Atkinson, R.J. Watts, Water Res. 35 (2001) 977–984.
[4] R. Andreozzi, V. Caprio, R. Marotta, Water Res. 36 (2002) 2761–2768.
[5] R. Andreozzi, A. D'Apuzzo, R. Marotta, Water Res. 36 (2002) 4691–4698.
[6] W.P. Kwan, B.M. Voelker, Environ. Sci. Technol. 38 (2004) 3425–3431.
[7] J.J. Pignatello, E. Oliveros, A. MacKay, Crit. Rev. Environ. Sci. Technol. 36 (2006) 1–84.
[8] D.Q. Wu, G.Y. Diao, P. Yuan, B. Min. Petrol. Geochem. 25 (2006) 293–298.
[9] R. Matta, K. Hanna, S. Chiron, Sci. Total Environ. 385 (2007) 242–251.
[10] Y.T. Lin, M.C. Lu, Water Sci. Technol. 55 (12) (2007) 101–106.
[11] J. Bandara, J.A. Mielczarski, A. Lopez, J. Kiwi, Appl. Catal. B: Environ. 34 (2001) 321–333.
[12] S.S. Lin, M.D. Gurol, Environ. Sci. Technol. 32 (1998) 1417–1423.
[13] R. Chen, J.J. Pignatello, Environ. Sci. Technol. 31 (1997) 2399–2406.
[14] R. Siegel, J.R. Howell, Thermal Radiation Heat Transfer, 4th ed., Hemisphere Publishing Corp., Bristol, PA, 2002.
[15] C.R. Esterkin, A.C. Negro, O.M. Alfano, A.E. Cassano, AlChE J. 51 (2005) 2298–2310.
[16] S.L. Murov, I. Carmichael, G.I. Hug, Handbook of Photochemistry, second ed., Marcel Dekker, Inc., New York, 1993.
[17] C.S. Zalazar, M.D. Labas, C.A. Martin, R.J. Brandi, O.M. Alfano, A.E. Cassano, Chem. Eng. J. 109 (2005) 67–81.
[18] R.M. Cornell, U. Schwertmann, The Iron Oxides: Structure, Properties, Reactions, Occurrences and Uses, Wiley VCH, Weinheim, 2003.
[19] J.S. LaKind, A.T. Stone, Geochim. Cosmochim. Acta 53 (1989) 961–971.
[20] N. Kang, D.S. Lee, J. Yoon, Chemosphere 47 (2002) 915–924.
[21] J. Ma, W. Song, C. Chen, M. Cheng, W. Ma, J. Zhao, Y. Tang, Environ. Sci. Technol. 39 (2005) 5810–5815.
[22] B.W. Wojciechowski, N.M. Rice, Experimental Methods in Kinetic Studies, Elsevier, Amsterdam, The Netherlands, 2003.
[23] S.-S. Lin, Interaction of H(2)O(2) with iron oxide for oxidation of organic compounds in water, Ph.D. Thesis, Drexel University, 1997.
[24] K.A. Levenberg, Q. Appl. Math. 2 (1944) 164–168.
[25] D. Marquardt, SIAM J. Appl. Math. 11 (1963) 431–441.
[26] A.E. Cassano, C.A. Martin, R.J. Brandi, O.M. Alfano, Ind. Eng. Chem. Res. 34 (1995) 2155–2201.
[27] O.M. Alfano, R.L. Romero, A.E. Cassano, Chem. Eng. Sci. 41 (1986) 1155–1161.
[28] O.M. Alfano, A.C. Negro, M.I. Cabrera, A.E. Cassano, Ind. Eng. Chem. Res. 34 (1995) 488–499.
[29] J.J. Duderstadt, R. Martin, Transport Theory, Wiley, New York, 1979.
[30] R.J. Brandi, M.A. Citroni, O.M. Alfano, A.E. Cassano, Chem. Eng. Sci. 58 (2003) 979–985.
[31] M.N. Ozisik, Radiative Transfer and Interactions with Conduction and Convection, J. Wiley, New York, 1973.
[32] A.R. Tymoschuk, A.C. Negro, O.M. Alfano, A.E. Cassano, Ind. Eng. Chem. Res. 32 (1993) 1342–1353.
[33] B.C. Faust, J. Hoigne, Atmos. Environ. Part A Gen. Top. 24 A (1990) 79–89.